Supplementary Information (SI) for Journal of Materials Chemistry A.

# Supporting Information

## Charge transfer cocrystal hydrogels for solar-driven lithium extraction and water co-generation

Wenzhe Sun, †[a] Jianxing Gu, †[a] Shihan Zhang, [a] Yi Su,[a] Lingjie Sun,[a*] Xiaotao Zhang,[a] Fangxu Yang,[a] Jing Feng,[b] Ran Ding,[b*] and Wenping Hu,[a,c*]

[a]State Key Laboratory of Advanced Materials for Intelligent Sensing, Key Laboratory of Organic Integrated Circuit, Ministry of Education & Tianjin Key Laboratory of Molecular Optoelectronic Sciences, Department of Chemistry, School of Science & Institute of Molecular Aggregation Science, Tianjin University, Tianjin 300072, China.

[b]State Key Laboratory of Integrated Optoelectronics, College of Electronic Science and Engineering, Jilin University, Changchun 130012, China.

[c]College of Chemistry and Chemical Engineering, Xiamen University, Fujian 361005, China.

†These authors contributed equally to this work.

Email address:

sunlingjie@tju.edu.cn (Sun L);

dingran@jlu.edu.cn (Ding R);

huwp@tju.edu.cn (Hu W).

## Calculation of the photothermal conversion efficiency

The photothermal energy conversion performance (denoted as $\eta$) for the ATQ cocrystal was evaluated following established methodologies. The overall energy conservation of the measurement system is described by the following differential equation:

$$\sum_i m_i C_{p,i} \frac{dT}{dt} = Q_s - Q_{loss}$$

Herein, $m_i$ refers to the weight of the test sample (100 mg), and $C_{p,i}$ stands for its specific heat capacity [1.327 J·(g·°C)$^{-1}$] (Fig. S13). The parameter $Q_S$ signifies the thermal energy generated from the incident laser, while $Q_{loss}$ corresponds to the heat dissipated into the ambient environment.

Upon reaching the maximum temperature plateau, the system achieves a thermal steady state, meaning the heat gain perfectly matches the heat dissipation:

$$Q_s = Q_{loss} = hS\Delta T_{max}$$

In this expression, $h$ acts as the heat transfer coefficient, $S$ is the effective surface area exposed to the environment, and $\Delta T_{max}$ denotes the peak temperature elevation.

Consequently, the value of $\eta$ is derived using the formula below:

$$\eta = \frac{hS\Delta T_{\max}}{I\left(1-10^{-A}\right)}$$

where $I$ indicates the power density of the applied laser (0.6 W·cm$^{-2}$), and $A$ (0.81) represents the absorbance of the target material at the specific wavelength of 808 nm.

To determine the unknown $hS$ value, a dimensionless temperature parameter ($\theta$) is defined:

$$\theta = \frac{T - T_{\text{surr}}}{T_{\max} - T_{\text{surr}}}$$

where $T$ tracks the transient temperature, $T_{max}$ is the steady-state maximum temperature, and $T_{surr}$ implies the baseline ambient temperature.

Additionally, the system's time constant ($\tau_s$) is formulated as:

$$\tau_s = \frac{\sum_i m_i C_{p,i}}{hS}$$

Combining the relationships above, the temperature variation rate is given by:

$$\frac{d\theta}{dt}=\frac{1}{\tau_s}\left(\frac{Q_s}{hS\Delta T_{\max}}\right)-\frac{\theta}{\tau_s}$$

During the natural cooling phase (once the laser is turned off), the heat input ceases ( $Q_s =$ 0). This simplifies the differential equation to $\frac{d\theta}{dt}=-\frac{\theta}{\tau_s}$, which integrates to $t=-\tau_s ln\theta$. Thus, by plotting the cooling time t against $-ln\theta$, the value of $\tau_s$ can be directly extracted from the slope, enabling the calculation of $hS$.

Based on this analytical model, the measured $\tau_s$ is 29.58 s. Ultimately, the photothermal conversion efficiency ($\eta$) of ATQ cocrystal under 808 nm irradiation is determined to be 76.63%.[1-3]

# Calculations of Lithium Adsorption Performance

## 1. Adsorption Capacity

The amounts of $Li^+$ adsorbed by the LEH at equilibrium ($q_e$, mg $g^{-1}$) were calculated based on the mass balance equations as follows:

$$q_e = \frac{(C_0 - C_e)V}{m}$$

where $C_0$ (mg $L^{-1}$) is the initial concentration of $Li^+$ in the solution, $C_e$ (mg $L^{-1}$) is the equilibrium concentration of $Li^+$ after adsorption. $V$ (L) represents the volume of the testing solution, and $m$ (g) corresponds to the dry mass of the active adsorbent within the LEH. The concentrations of $Li^+$ and other co-existing ions were determined utilizing Inductively Coupled Plasma Optical Emission Spectrometry (ICP-OES).[4, 5]

## 2. Distribution Coefficient and Selectivity

To evaluate the specific selectivity of the LEH towards $Li^+$ against the primary competing ion, $Mg^{2+}$, in simulated high-magnesium brines, the distribution coefficients ($K_d$, mL $g^{-1}$) for both ions and the separation factor ($S_{Li/Mg}$) were determined using the following equations:

$$K_d^{Li} = \frac{C_0^{Li} - C_e^{Li}}{C_e^{Li}} \times \frac{V}{m}$$

$$K_d^{Mg} = \frac{C_0^{Mg} - C_e^{Mg}}{C_e^{Mg}} \times \frac{V}{m}$$

$$S_{Li/Mg} = \frac{K_d^{Li}}{K_d^{Mg}}$$

where $C_0^{Li}$ and $C_0^{Mg}$ (mg $L^{-1}$) are the initial concentrations of $Li^+$ and $Mg^{2+}$ in the solution, respectively. $C_e^{Li}$ and $C_e^{Mg}$ (mg $L^{-1}$) represent their corresponding equilibrium concentrations after the adsorption process. $V$ (L) is the volume of the testing solution, and $m$ (g) corresponds to the dry mass of the active adsorbent within the LEH. $K_d^{Li}$ and $K_d^{Mg}$ represent the distribution coefficients of $Li^+$ and $Mg^{2+}$, respectively. A remarkably high $S_{Li/Mg}$ value signifies the extraordinary preferential binding affinity and precise size-exclusion capability of the LEH for $Li^+$ over $Mg^{2+}$.[6, 7]

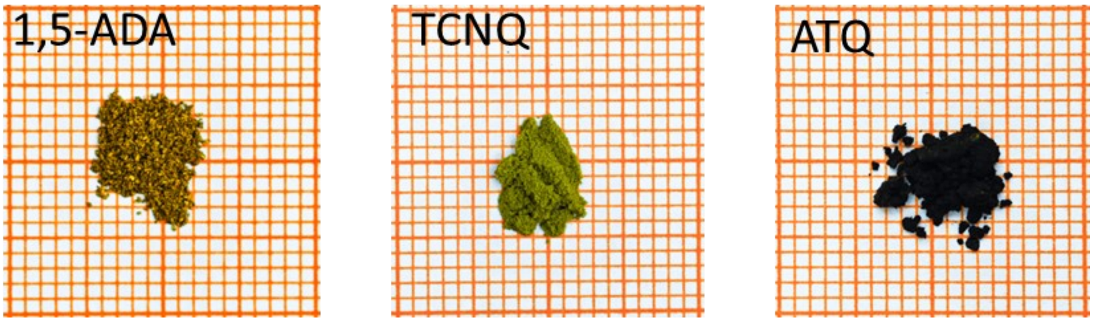

**Figure S1.** Optical photographs of 1,5-ADA, TCNQ, and ATQ crystals under ambient conditions.

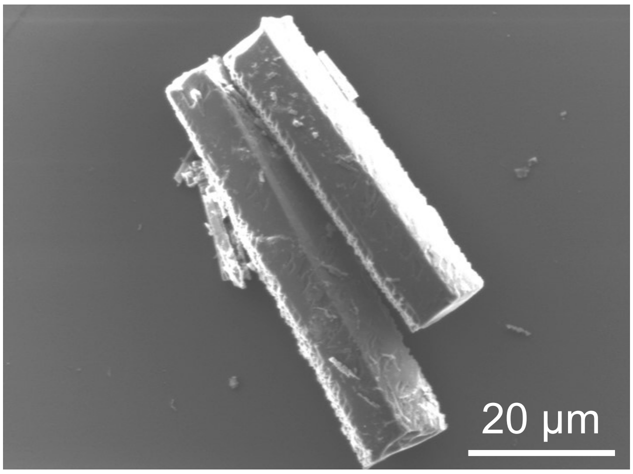

**Figure S2.** Scanning electron microscopy (SEM) image of the ATQ cocrystal.

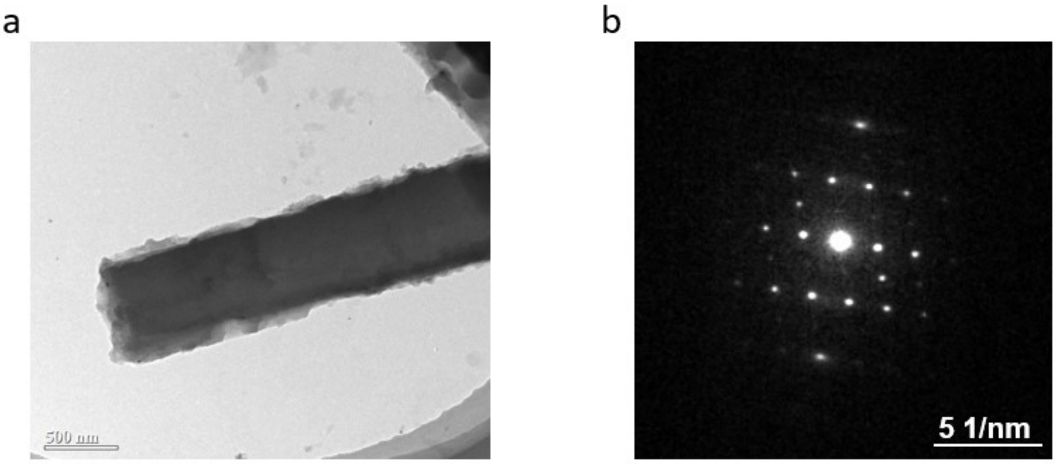

**Figure S3.** (a) TEM image of the individual ATQ cocrystal microrods. (b) The SAED pattern of this cocrystal microrod. Scale bars: 500 nm in (a) and 5 1/nm in (b).

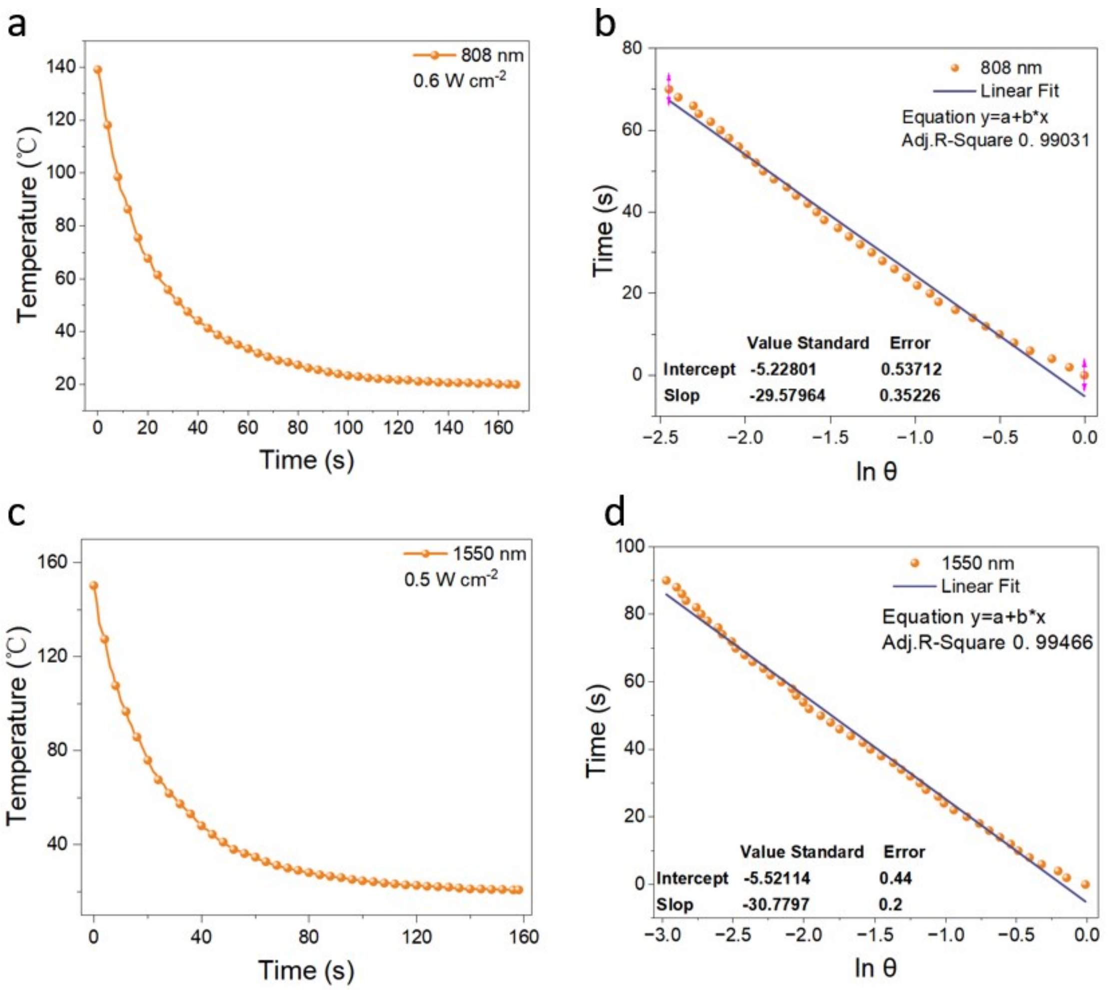

**Figure S4.** The cooling curve of ATQ cocrystal under the irradiation of (a) 808 nm laser, (c) 1550 nm laser. The corresponding time-ln θ linear curve (b) 808 nm, (d) 1550 nm.

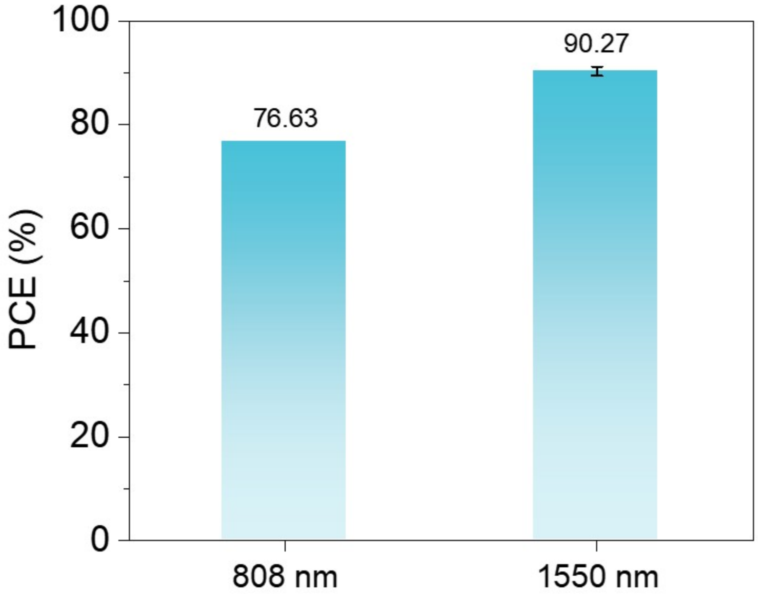

**Figure S5.** Photothermal conversion efficiencies of ATQ under laser irradiation at different wavelengths.

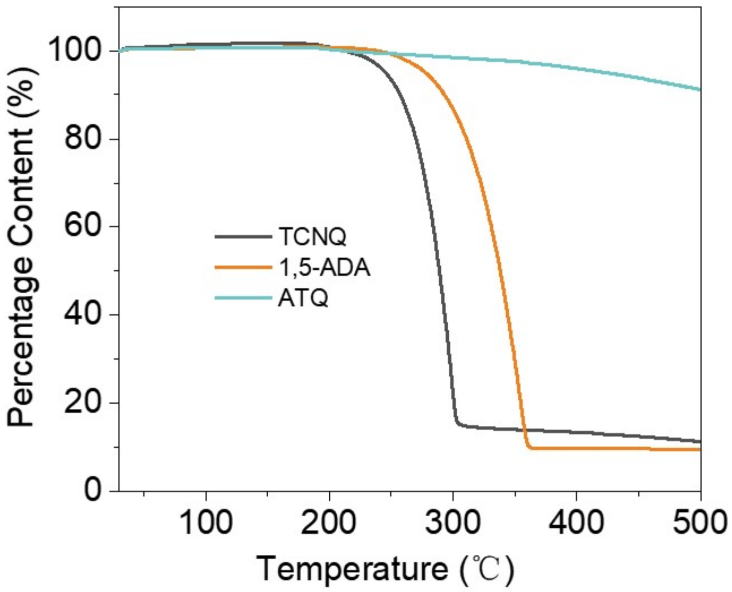

**Figure S6.** Thermogravimetric analysis (TGA) curve of TCNQ, 1,5-ADA and ATQ.

**Figure S7.** Photographs of the LEH before, during, and after a static compression test under a 500 g weight for 10 min.

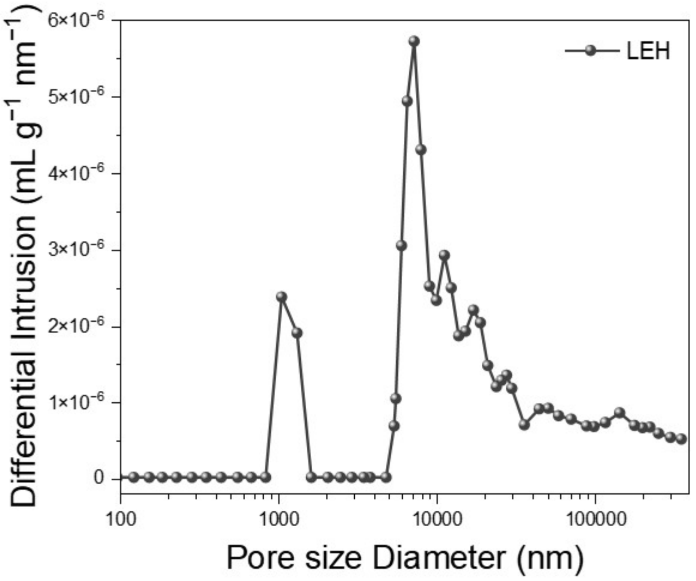

**Figure S8.** Pore size distribution of LEH measured by mercury intrusion porosimetry (MIP)

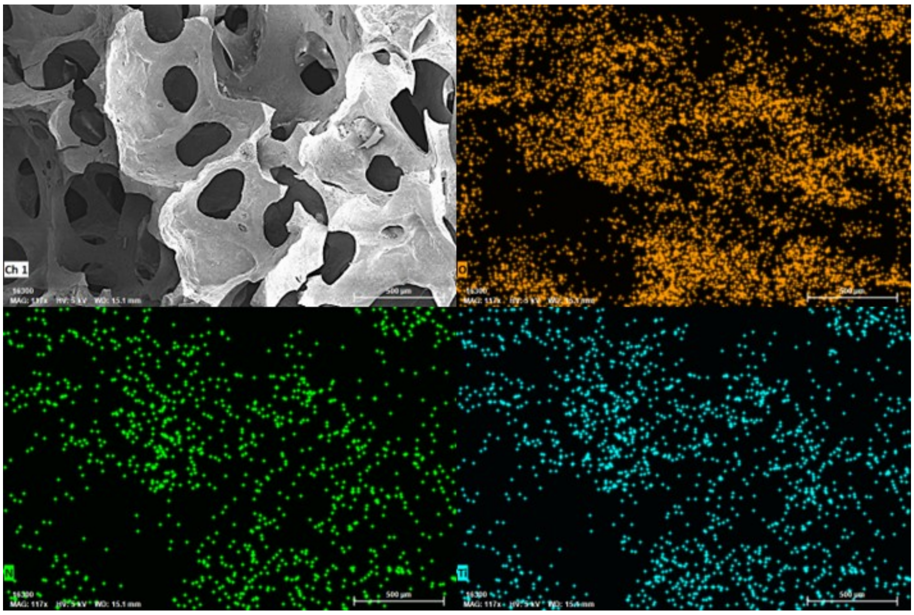

**Figure S9.** SEM image and the corresponding EDS elemental mapping of LEH, showing the spatial distribution of O, N, and Ti elements. O, N, and Ti are marked in orange, green, and blue, respectively.

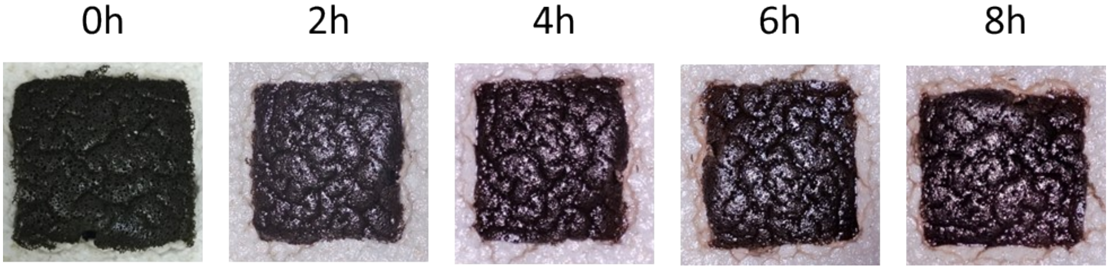

**Figure S10.** Time-dependent photographs of surface salt crystallization on LEH in simulated high-salinity brine under 1 sun illumination. (Ion concentration: $K^+$ 11497 ppm, $Mg^{2+}$ 10593 ppm, $Na^+$ 5613 ppm, $Ca^{2+}$ 715.3 ppm)

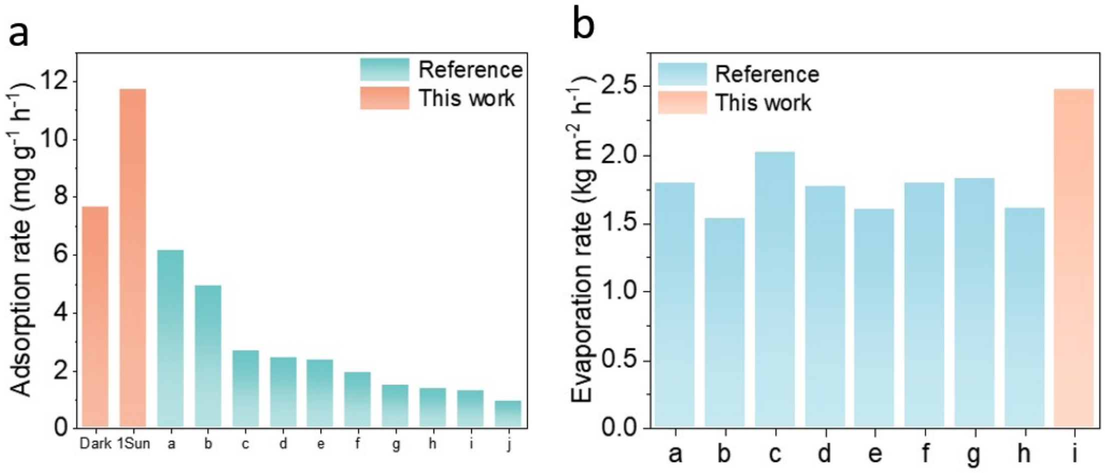

**Figure S11.** Comparison of (a) apparent $Li^+$ adsorption rates and (b) evaporation rates between the ATQ-based LEH and reported systems.

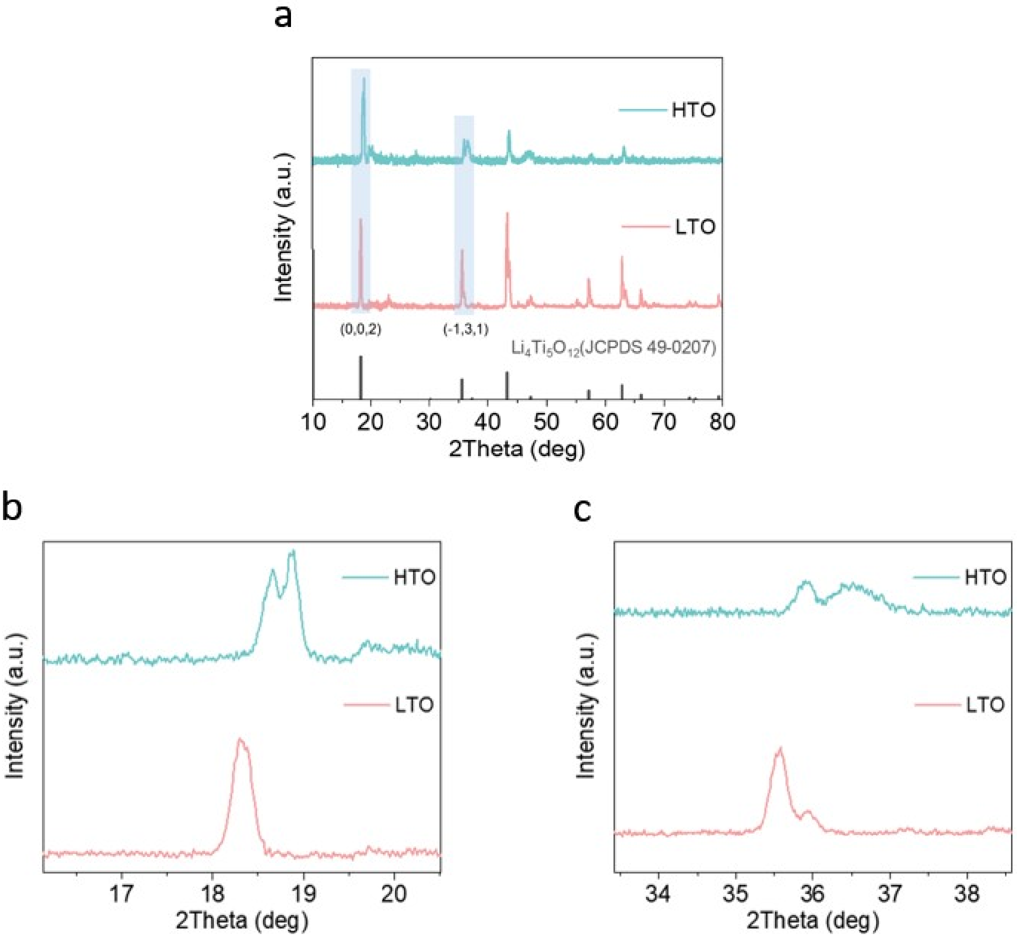

**Figure S12.** PXRD characterization of LTO and HTO. (a) Full-range PXRD patterns of LTO and HTO with the standard reference pattern; (b, c) enlarged PXRD patterns in the 2θ regions of 16–20.5° and 33.5–38.5°, respectively.

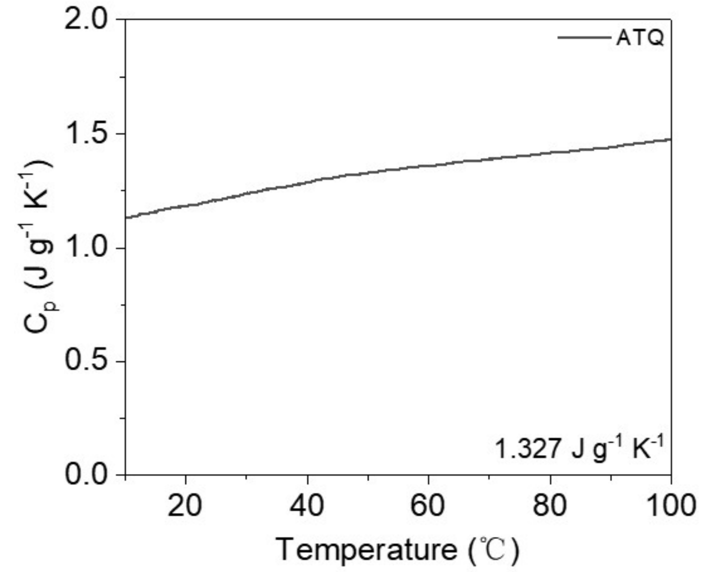

**Figure S13.** Temperature-dependent specific heat capacity ($C_p$) of the ATQ cocrystal measured by differential scanning calorimetry (DSC) using the sapphire method.

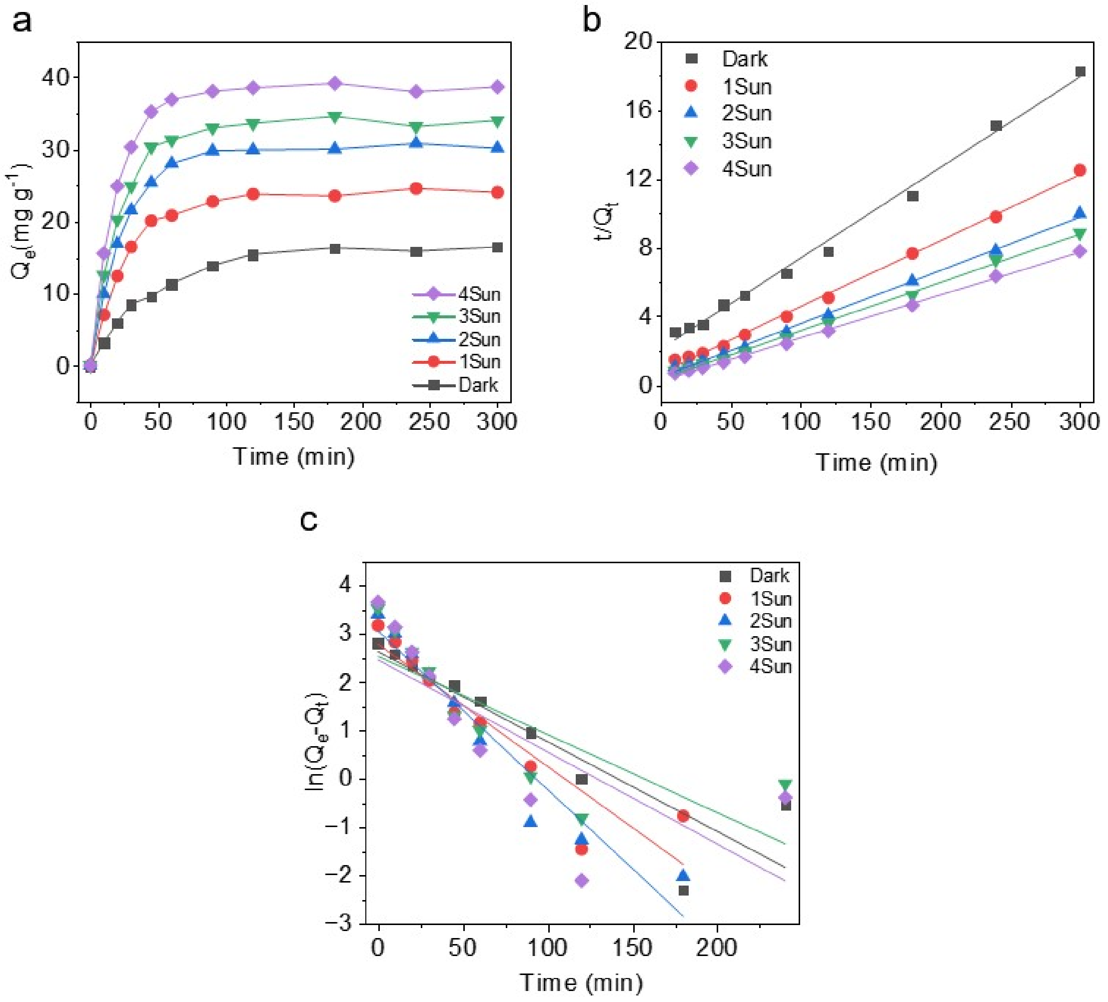

**Figure S14.** $Li^+$ adsorption kinetics of LEH under different irradiation intensities: (a) time-dependent adsorption capacities, (b) pseudo-second-order fitting plots, and (c) pseudo-first-order fitting plots.

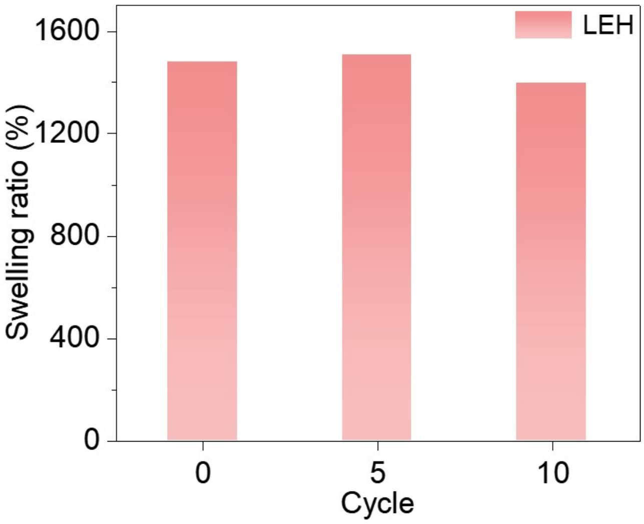

**Figure S15.** Swelling ratios of LEH after 0, 5, and 10 adsorption–desorption cycles.

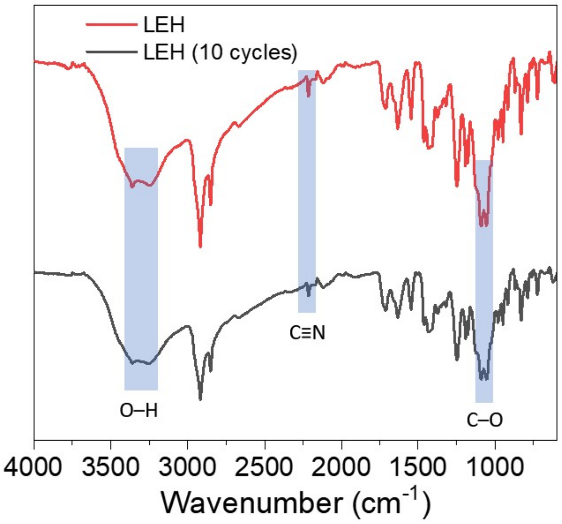

**Figure S16.** FTIR spectra of pristine LEH and LEH after 10 adsorption–desorption cycles.

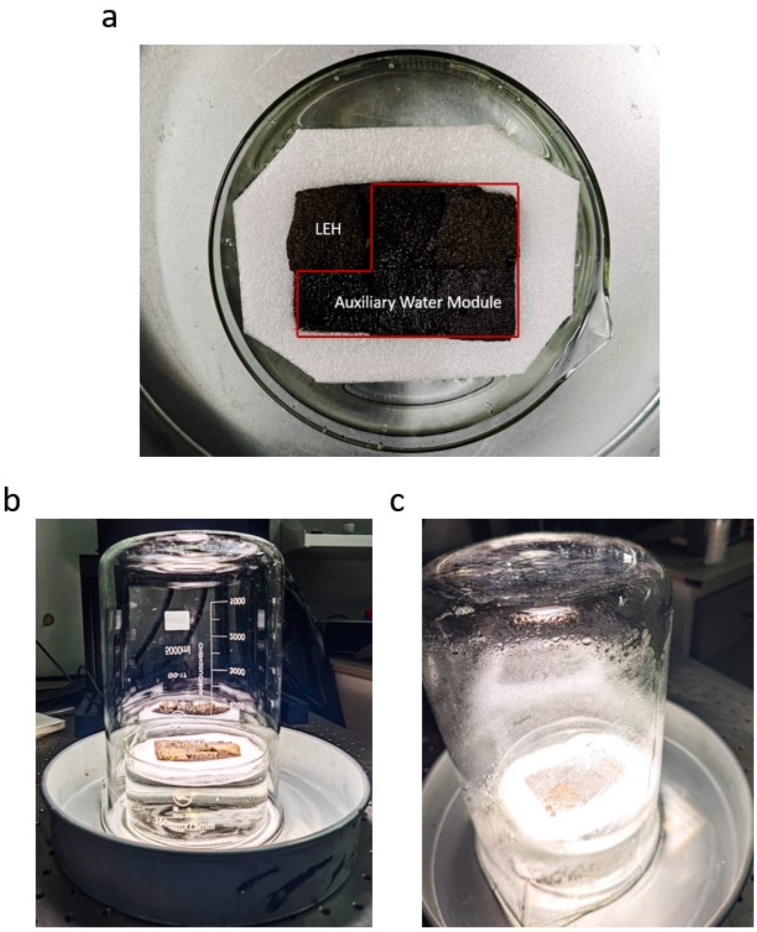

**Figure S17.** Condensate collection setup for module-assisted freshwater generation: (a) photograph of LEH coupled with the auxiliary water module, (b) photograph of the condensate collection device, and (c) water vapor condensation on the inner wall during operation.

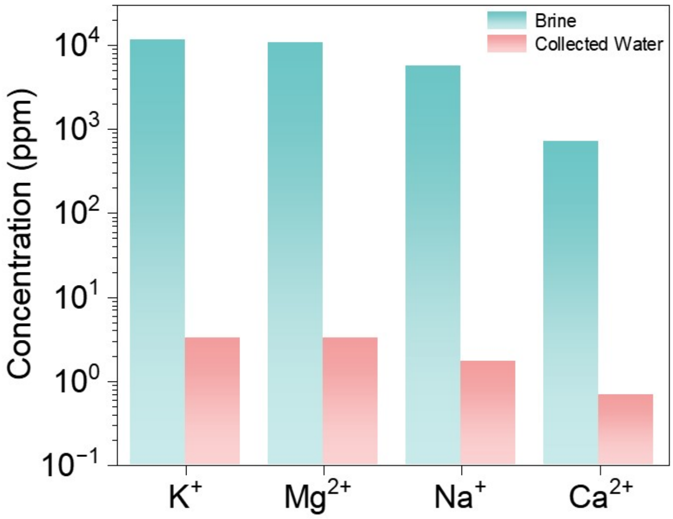

**Figure S18.** A water quality analysis of collected condensate and brine.

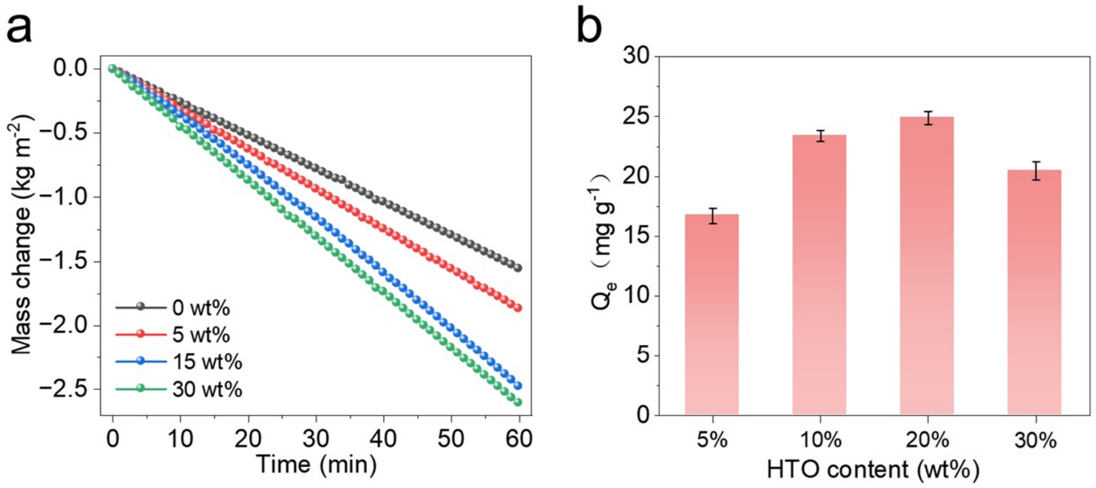

**Figure S19.** Optimization of LEH composition: (a) Evaporation performance of hydrogels with different ATQ loadings and (b) $Li^+$ adsorption capacities of hydrogels with different HTO loadings.

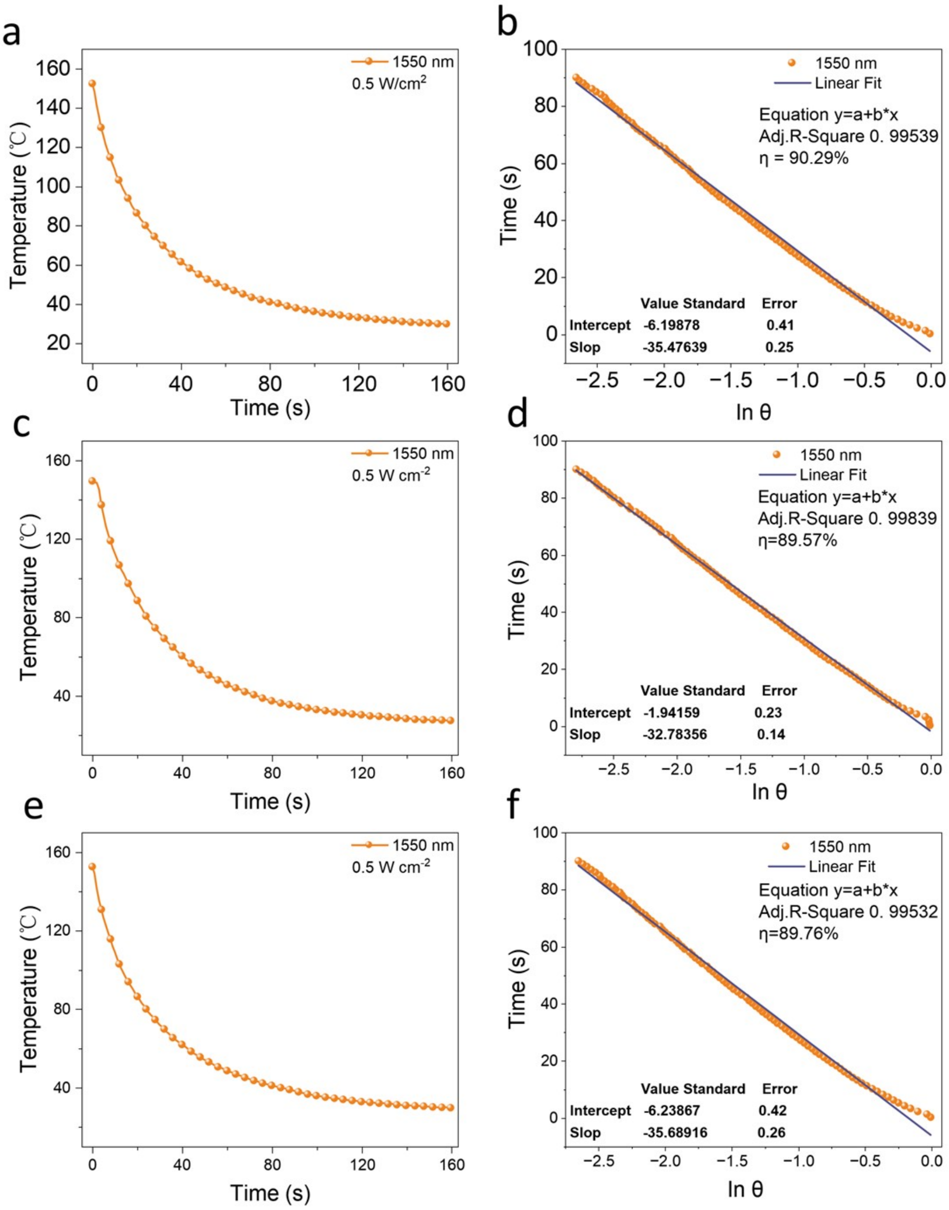

**Figure S20.** PCE analysis of ATQ under 1550 nm irradiation. (a, c, e) Cooling profiles and (b, d, f) corresponding linear fittings from three independent measurements.

**Table S1.** Crystal data and structure refinement for cocrystal of ATQ.

| Parameter | Value/Comment |
|---|---|
| CCDC number | 2542698 |
| Empirical formula | C13H8N3 |
| Formula weight | 206.22 |
| Wavelength | 1.54184 Å |
| Crystal system | monoclinic |
| Space group | *P*21/*n* |
| Unit cell dimensions | *a*=6.9890(2) Å |
| | *b*=8.2781(3) Å |
| | *c*=17.2223(5) Å |
| | *α*=90° |
| | *β*=99.172(3)° |
| | *γ*=90° |
| Volume | 983.67(5) Å$^3$ |
| Z | 4 |
| Density | 1.393 g/cm$^3$ |
| Absorption Coefficient | 0.688 mm$^{-1}$ |
| F（000） | 428 |
| Theta range for data collection | 2.580°~74.925° |
| Index range | -8≤*h*≤8 |
| | -9≤*k*≤9 |
| | -20≤*l*≤20 |
| Reflections collected | 25608 |
| Independent reflections | 1740[R(int)=0.0972] |
| R indices (all data) | R=0.0619 wR=0.1455 |

**Table S2.** Compositions of LiCl-$MgCl_2$ mixtures with a fixed salinity of 20.0 g $L^{-1}$ and varying $Mg^{2+}$/$Li^+$ ratios.

| $Mg^{2+}$: $Li^+$ ratio of solution | LiCl concentration (mg/L) | $Li^+$ concentration (mg/L) | $MgCl_2$ concentration (mg/L) | $Mg^{2+}$ concentration (mg/L) | Total salinity (g/L) |
|---|---|---|---|---|---|
| 10 | 2698 | 442 | 17302 | 4417 | 20 |
| 20 | 1446 | 237 | 18554 | 4736 | |
| 40 | 750 | 123 | 19250 | 4914 | |
| 80 | 382 | 62.6 | 19618 | 5008 | |
| 160 | 193 | 31.6 | 19807 | 5056 | |

**Table S3.** Ionic composition of the simulated salt-lake brine used in this study.

| $K^+$ (mg/L) | $Mg^{2+}$ (mg/L) | $Na^+$ (mg/L) | $Ca^{2+}$ (mg/L) |
|---|---|---|---|
| 11497 | 10593 | 5613 | 715.3 |

**Table S4.** Comparison of $Li^+$ adsorption kinetics with reported lithium extraction systems.

| Number | Adsorption capacity ($mg\ g^{-1}$) | Time (h) | Adsorption rate ($mg\ g^{-1}\ h^{-1}$) | Reference |
|---|---|---|---|---|
| a | 18.44 | 3 | 6.15 | 8 |
| b | 59.10 | 12 | 4.93 | 9 |
| c | 10.64 | 4 | 2.66 | 10 |
| d | 9.72 | 4 | 2.43 | 11 |
| e | 18.60 | 8 | 2.33 | 12 |
| f | 2.88 | 1.5 | 1.92 | 13 |
| g | 35.43 | 24 | 1.48 | 14 |
| h | 12.02 | 9 | 1.34 | 15 |
| i | 31.03 | 24 | 1.29 | 16 |
| j | 11.00 | 12 | 0.92 | 17 |
| Dark | 15.28 | 2 | 7.64 | This work |
| 1Sun | 23.40 | 2 | 11.70 | |

**Table S5.** Comparison of evaporation rates of representative solar-driven evaporation systems.

| Number | System | Evaporation rate ($kg\ m^{-2}\ h^{-1}$) | Reference |
|---|---|---|---|
| a | Graphene oxide film with EPS foam | 1.79 | 18 |
| b | Carbon nanotubes with PS foam | 1.53 | 19 |
| c | PPy coated sponge with PS foam | 2.02 | 20 |
| d | umbrella-shaped evaporator | 1.77 | 21 |
| e | Hanging-model evaporator with PDA modified carbon-fiber | 1.60 | 22 |
| f | Hanging-model evaporator | 1.79 | 23 |
| g | Porous structure with carbon black | 1.83 | 24 |
| h | Heatsink-like evaporator | 1.61 | 25 |
| i | PVA hydrogel with ATQ cocrystal | 2.48 | This work |

**Table S6.** Comparison of Mg/Li separation performance with representative lithium extraction systems.

| System | Test condition | Mg/Li separation value | Reference |
|---|---|---|---|
| Al-doped $H_2TiO_3$ | Lagoco salt-lake brine | 48.49 | 26 |
| bifunctionally modified ion-sieve adsorbent | $Li^+ \approx 1.41$ g $L^{-1}$, $Mg^{2+} \approx 42.35$ g $L^{-1}$, Mg/Li ≈ 30 | 62.3 | 27 |
| Ti-based LIS nanofibers | Brine water | 125 | 9 |
| PA membrane | LiCl/$MgCl_2$ binary solution; total salt concentration = 10–80 g $L^{-1}$; $MgCl_2$/LiCl mass ratio = 1:1 | 16.2 | 28 |
| HTO + ATQ/PVA hydrogel | Total salinity = 20 g $L^{-1}$; $Mg^{2+}/Li^+$ mass ratio = 160; | 180 | This work |

**Table S7.** Kinetic fitting parameters for $Li^+$ adsorption under different irradiation intensities.

| R$^2$<br>Condition | Pseudo-First-Order | Pseudo-Second-Order |
|---|---|---|
| Dark | 0.7932 | 0.9936 |
| 1Sun | 0.8401 | 0.9967 |
| 2Sun | 0.9221 | 0.9971 |
| 3Sun | 0.5825 | 0.9974 |
| 4Sun | 0.5004 | 0.9981 |

## Reference

1. Y. Su, Z. Zheng, L. Sun, W. Sun, Y. Zhang, H. Liu, C. Yang, S. Li, M. Wang and X. Chen, *Sci. China Mater.*, 2025, **68**, 3203-3211.
2. S. Tian, H. Bai, S. Li, Y. Xiao, X. Cui, X. Li, J. Tan, Z. Huang, D. Shen and W. Liu, *Angew. Chem.*, 2021, **133**, 11864-11868.
3. Y. Wang, W. Zhu, W. Du, X. Liu, X. Zhang, H. Dong and W. Hu, *Angew. Chem.*, 2018, **130**, 4027-4031.
4. Y. Wang, W. Zhao, Z. Peng, Y. Feng, J. Lu, Y. Song, W. Xu, X. Wen, Z. Chen and Z. Wang, *Adv. Mater.*, 2025, **37**, 2502134.
5. Z. Yu, Z. Mao, S. Guo, Y. Li, X. Cheng, C. Li, L. Li, F. Duan, W. Li and Y. Zhang, *Nat. Commun.*, 2025, **16**, 8825.
6. Q. Xia, Z. Deng, S. Sun, W. Zhao, J. Ding, B. Xi, G. Gao and C. Wang, *Proc. Natl. Acad. Sci.*, 2024, **121**, e2400159121.
7. W. Xing, D. Wang, K. Feng, S. Ding, X. Zhang, H. Xu, J. Gong, J. Qu and R. Niu, *Energy Environ. Sci.*, 2025, **18**, 10102-10111.
8. X. Chen, W. Yu, Y. Zhang, C. Huang, L. Nie, J. Yu, Y. Zhang, C. Zhang, W. Zhai and X. Zhang, *Adv. Funct. Mater.*, 2024, **34**, 2316178.
9. S. Wei, Y. Wei, T. Chen, C. Liu and Y. Tang, *Chem. Eng. J.*, 2020, **379**, 122407.
10. C. Liu, B. Tao, Z. Wang, D. Wang, R. Guo and L. Chen, *Chem. Eng. Sci.*, 2021, **229**, 115984.
11. J. Chen, C. Lian, J. Yu and S. Lin, *AIChE J.*, 2024, **70**, e18280.
12. L. Tang, S. Huang, Y. Wang, D. Liang, Y. Li, J. Li, Y. Wang, Y. Xie and W. Wang, *ACS applied materials & interfaces*, 2020, **12**, 9775-9781.
13. X. Chen, C. Wu, Y. Lv, C. Zhang, X. Zhang, L. Nie, Y. Zhang, L. Zhao, C. Huang and W. Liu, *Matter*, 2022, **5**, 3053-3065.
14. S. M. Hossain, I. Ibrahim, Y. Choo, A. Razmjou, G. Naidu, L. Tijing, J.-H. Kim and H. K. Shon, *Desalination*, 2022, **525**, 115491.
15. Z. Zhu, H. Li, Z. Wang, X. Yue, T. Zhang and F. Qiu, *Chem. Eng. Sci.*, 2025, **318**, 122145.
16. G. Zhang, C. Hai, Y. Zhou, W. Tang, J. Zhang, J. Zeng, Y. Liu, S. Dong and G. Peng, *Chem. Eng. J.*, 2022, **450**, 137912.
17. L. A. Limjuco, G. M. Nisola, C. P. Lawagon, S.-P. Lee, J. G. Seo, H. Kim and W.-J. Chung, *Colloids Surf. Physicochem. Eng. Aspects*, 2016, **504**, 267-279.
18. M. Xie, P. Zhang, Y. Cao, Y. Yan, Z. Wang and C. Jin, *npj Clean Water*, 2023, **6**, 12.
19. H. W. Lim and S. J. Lee, *Desalination*, 2022, **526**, 115540.
20. B. Peng, Q. Lyu, M. Li, S. Du, J. Zhu and L. Zhang, *Adv. Funct. Mater.*, 2023, **33**, 2214045.
21. Y. Dong, J. a. Wang, K. Wang, C. Li, Y. Cai, J. Li, S. S. Lam and C. Sonne, *J. Clean Prod.*, 2023, **418**, 138024.
22. X. Li, W. Xu, M. Tang, L. Zhou, B. Zhu, S. Zhu and J. Zhu, *Proc. Natl. Acad. Sci.*, 2016, **113**, 13953-13958.
23. J. Wang, Q. Shi, C. Li, Y. Zhang, S. Du, J. Mao and J. Wang, *Adv. Funct. Mater.*,

2022, **32**, 2201922.

24. H. Zhang, X. Shen, E. Kim, M. Wang, J. H. Lee, H. Chen, G. Zhang and J. K. Kim, *Adv. Funct. Mater.*, 2022, **32**, 2111794.
25. E. Yang, N. Wei, M. Li, R. Xu, Y. Sui, M. Kong, X. Ran and H. Cui, *ACS applied materials & interfaces*, 2022, **14**, 29788-29796.
26. X. Dai, H. Zhan, Z. Qian, J. Li, Z. Liu and Z. Wu, *RSC Adv.*, 2021, **11**, 34988-34995.
27. J. Zhang, Z. Cheng, X. Qin, X. Gao, R. Yun and X. Xiang, *ACS Applied Materials & Interfaces*, 2023, **15**, 29586-29596.
28. S. Zhang, X. Wei, X. Cao, M. Peng, M. Wang, L. Jiang and J. Jin, *Nat. Commun.*, 2024, **15**, 238.